Article

One-dimensional Luttinger liquids in a two-dimensional moiré lattice

https://doi.org/10.1038/s41586-022-04514-6

Received: 16 March 2021

Accepted: 3 February 2022

Published online: 4 May 2022

Check for updates

Pengjie Wang[1,10], Guo Yu[1,2,10], Yves H. Kwan[3,10], Yanyu Jia[1], Shiming Lei[4,5], Sebastian Klemenz[4,6], F. Alexandre Cevallos[4], Ratnadwip Singha[4], Trithep Devakul[7], Kenji Watanabe[8], Takashi Taniguchi[9], Shivaji L. Sondhi[1,3], Robert J. Cava[4], Leslie M. Schoop[4], Siddharth A. Parameswaran[3] & Sanfeng Wu[1]✉

The Luttinger liquid (LL) model of one-dimensional (1D) electronic systems provides a powerful tool for understanding strongly correlated physics, including phenomena such as spin–charge separation[1]. Substantial theoretical efforts have attempted to extend the LL phenomenology to two dimensions, especially in models of closely packed arrays of 1D quantum wires[2–13], each being described as a LL. Such coupled-wire models have been successfully used to construct two-dimensional (2D) anisotropic non-Fermi liquids[2–6], quantum Hall states[7–9], topological phases[10,11] and quantum spin liquids[12,13]. However, an experimental demonstration of high-quality arrays of 1D LLs suitable for realizing these models remains absent. Here we report the experimental realization of 2D arrays of 1D LLs with crystalline quality in a moiré superlattice made of twisted bilayer tungsten ditelluride ($tWTe_2$). Originating from the anisotropic lattice of the monolayer, the moiré pattern of $tWTe_2$ hosts identical, parallel 1D electronic channels, separated by a fixed nanoscale distance, which is tuneable by the interlayer twist angle. At a twist angle of approximately 5 degrees, we find that hole-doped $tWTe_2$ exhibits exceptionally large transport anisotropy with a resistance ratio of around 1,000 between two orthogonal in-plane directions. The across-wire conductance exhibits power-law scaling behaviours, consistent with the formation of a 2D anisotropic phase that resembles an array of LLs. Our results open the door for realizing a variety of correlated and topological quantum phases based on coupled-wire models and LL physics.

In various coupled-wire models[2–13], one-dimensional (1D) quantum wires are placed in parallel with each other at an exactly fixed nanoscale distance, producing a two-dimensional (2D) or three-dimensional periodic system. In 2D, such perfectly arranged wires can, in principle, realize a strongly anisotropic non-Fermi liquid phase that resembles a Luttinger liquid (LL)[2–6]. When a perpendicular magnetic field is applied, new quantum Hall states[7–9] may also develop in such an array without the presence of a free 2D electron gas. This highly anisotropic setting is qualitatively different from conventional isotropic 2D electron systems. Experimentally realizing these interesting coupled-wire constructions is challenging, as they require a large number of identical nanowires to be strictly arranged in a crystalline array at both nano and microscopic scales. A route to overcome these difficulties is to use moiré superlattices of a twisted bilayer stack of an anisotropic 2D crystal. Indeed, it has been proposed that twisted 2D crystals with a rectangular unit cell, such as GeSe[14], create 1D flat bands. Another excellent choice is $tWTe_2$, as its monolayer unit cell is an elongated rectangle. In this work, we uncover the potential of $tWTe_2$ for creating the desired high-quality arrays of 1D wires that can expand the LL physics to 2D.

$tWTe_2$ moiré lattices and device design

Monolayer WTe_2 consists of three atomic layers (Te-W-Te) in a sandwich structure, in which the W atoms are organized in 1D zigzag chains[15] (Fig. 1a). The $tWTe_2$ hence has six atomic layers with a complicated moiré pattern. To better illustrate the moiré lattice of small-angle $tWTe_2$, we present the superlattice of only the W layers and of only the Te layers separately in Fig. 1b, c. The Te pattern develops a triangular superlattice viewed from the top, whereas the W moiré pattern develops 1D stripes, reflecting the underlying anisotropy of the monolayer. The bright stripes in Fig. 1b indicate regions where the W atoms from two layers are optimally aligned vertically (AA stripes), whereas in the dark stripes they are optimally misaligned (AB stripes). The distance d between neighbouring AA stripes depends on the twisted angle θ, $d = a/(2\sin(\theta/2))$, for small θ (Fig. 1d); here a is the length of the monolayer's rectangular unit cell. In Fig. 1e and Extended Data Fig. 1, we experimentally visualize this unique moiré structure of $tWTe_2$ using conductive atomic force microscopy (cAFM). Below we present transport studies of two devices with $\theta \approx 5^\circ$ ($d \approx 7.2$ nm, device no. 1) and $\theta \approx 6^\circ$ ($d \approx 6.0$ nm, device no. 2).

[1]Department of Physics, Princeton University, Princeton, NJ, USA. [2]Department of Electrical and Computer Engineering, Princeton University, Princeton, NJ, USA. [3]Rudolf Peierls Centre for Theoretical Physics, University of Oxford, Oxford, UK. [4]Department of Chemistry, Princeton University, Princeton, NJ, USA. [5]Department of Physics and Astronomy, Rice University, Houston, TX, USA. [6]Fraunhofer Research Institution for Materials Recycling and Resource Strategies IWKS, Hanau, Germany. [7]Department of Physics, Massachusetts Institute of Technology, Cambridge, MA, USA. [8]Research Center for Functional Materials, National Institute for Materials Science, Tsukuba, Japan. [9]International Center for Materials Nanoarchitectonics, National Institute for Materials Science, Tsukuba, Japan. [10]These authors contributed equally: Pengjie Wang, Guo Yu, Yves H. Kwan. ✉e-mail: sanfengw@princeton.edu

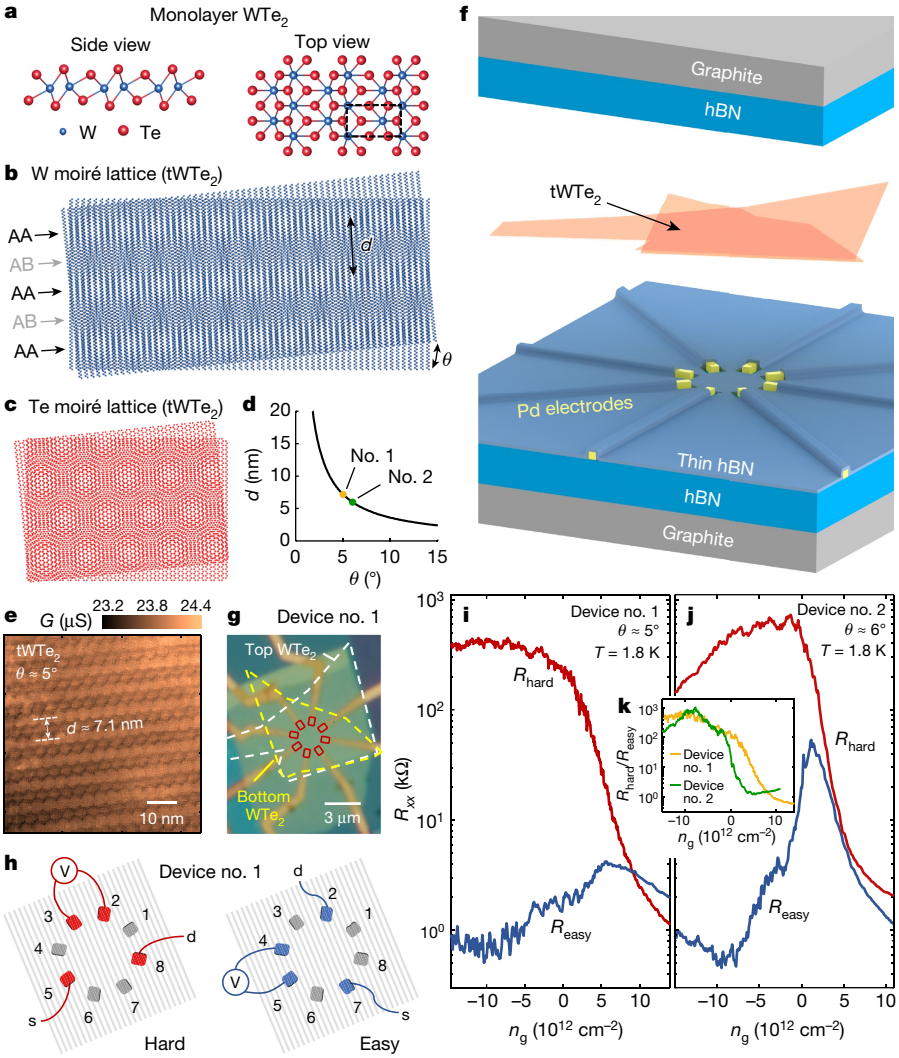

Fig. 1 | Small-angle $tWTe_2$ moiré lattices and large transport anisotropy. **a**, Crystal structure of monolayer WTe_2 (left: side view; right: top view). The dashed rectangle indicates the unit cell. **b**, Moiré superlattice of W atoms only, showing 1D channels (AA and AB stripes). **c**, Moiré superlattice of the Te atoms, showing a 2D triangular pattern. **d**, Calculated distance d between AA stripes shown in **b**, as a function of twist angle θ. The yellow (green) point indicates the parameter realized in device no. 1 (no. 2). **e**, A cAFM image of the $tWTe_2$ moiré structure (see details of the measurement in Extended Data Fig. 1 and Methods). **f**, Cartoon illustration of our $tWTe_2$ device design, in which a thin hBN layer with selectively etched areas is used to avoid electrical contact to non-$tWTe_2$ regions. **g**, An optical image of device no. 1. The dashed white (yellow) line highlights the top (bottom) monolayer WTe_2, and the red squares denote the contact regions. **h**, Cartoon illustration of the measurement configuration along hard and easy directions for device no. 1. The grey lines indicate the moiré stripes (not to scale). As an estimation, approximately 71 AA stripes exist between contacts 2 and 3. s, source; d, drain. **i**, Four-probe resistances measured with configurations shown in **h**, labelled as R_{hard} and R_{easy}, respectively, as a function of n_g for device no. 1 (cooldown no. 1) at 1.8 K. **j**, Similar four-probe resistances along easy and hard directions measured on device no. 2 (cooldown no. 1). **k**, The density-dependent anisotropy ratio, R_{hard}/R_{easy}, for the two devices, respectively.

Figure 1f illustrates the design of our devices for measuring the transport properties of $tWTe_2$. Similar to our previous reports[16,17], a thin hexagonal boron nitride (hBN) layer is inserted between the $tWTe_2$ and the palladium (Pd) electrodes, with selected areas etched in the thin hBN layer that expose the very ends of Pd for contacting the $tWTe_2$ bulk. Such a device geometry restricts the contact area to be small in the 2D bulk and eliminates transport contributions of conducting edges or any extra monolayer regions next to the stack. The $tWTe_2$ is fully encapsulated with hBN/graphite stacks from both top and bottom, which also act as the electrostatic gates. An optical image of a typical device is shown in Fig. 1g. We fabricate multiple contacts in a ring structure, which is key to investigating transport anisotropy. Details about the fabrication procedure are described in the Methods and Extended Data Fig. 2.

Exceptionally large transport anisotropy

We first examine transport anisotropy in the $tWTe_2$ devices. Figure 1i shows plots of the four-probe resistance R_{xx} as a function of gate-induced doping n_g, taken from device no. 1 at 1.8 K with the contact configurations (R_{hard} and R_{easy}) shown in Fig. 1h. Here $n_g \equiv \varepsilon_r\varepsilon_0(V_{tg}/d_{tg} + V_{bg}/d_{bg})/e$, where d_{tg} (d_{bg}) is the thickness of hBN dielectric layers for the top (bottom) gate; V_{tg} (V_{bg}) is the top (bottom) gate voltage; e, ε_0 and ε_r are the elementary charge, vacuum permittivity and relative dielectric constant of hBN, respectively. The current is applied along two orthogonal directions in the atomic plane for measuring R_{hard} and R_{easy}, respectively. The choice of the easy and hard directions was made by comprehensively examining two-probe resistances taken between all neighbouring electrodes and other configurations along and across moiré stripes (Extended Data

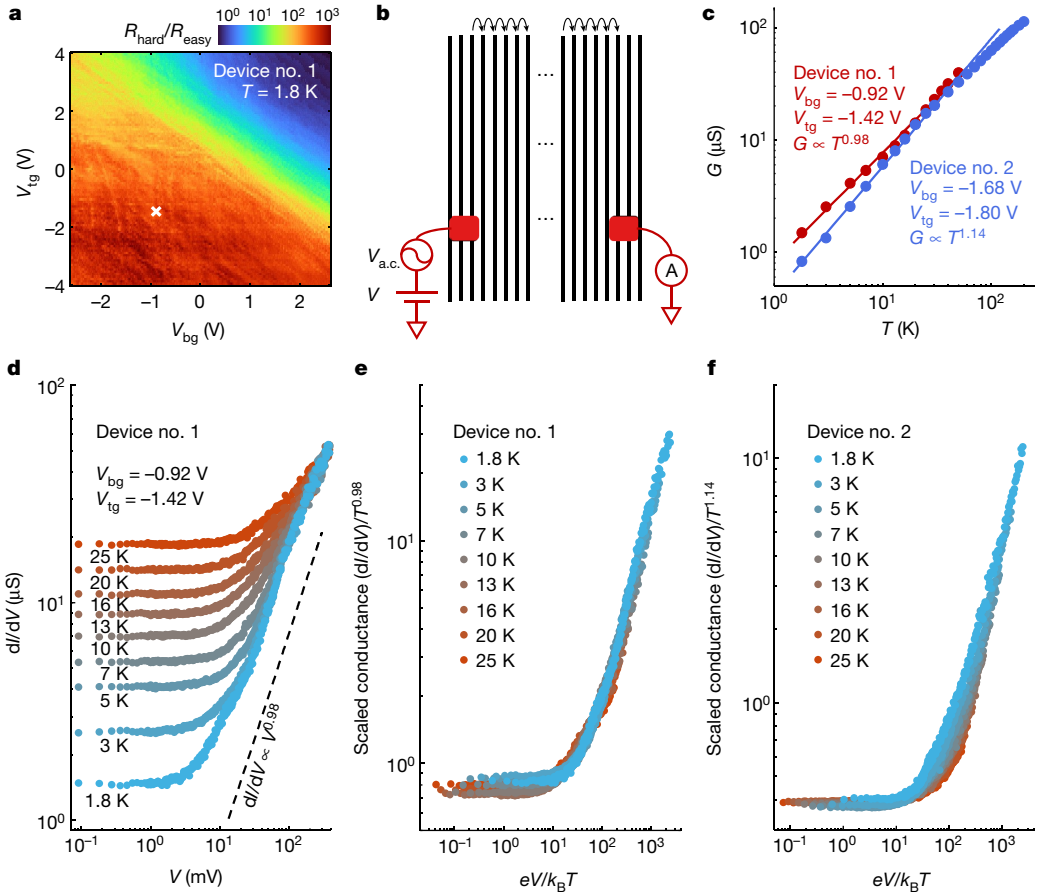

Fig. 2 | Luttinger liquid behaviours observed in the $tWTe_2$ devices. **a**, Dual-gate-dependent map of R_{hard}/R_{easy} measured in device no. 1 (cooldown no. 1) at 1.8 K. **b**, Illustration of the measurement configuration for determining two-probe across-wire conductance G and differential conductance dI/dV used in **c**–**f**. **c**, Across-wire conductance G as a function of T, plotted in log–log scale for device no. 1 (red) and no. 2 (blue) at a selected gate parameter indicated by the cross in **a**. The solid lines are the power-law fittings. **d**, Across-wire differential conductance dI/dV measured in device no. 1 as a function of d.c. bias V at different T. **e**, The same data as **d**, but plotted as a scaled conductance versus a scaled excitation. All data collapse to a single curve. **f**, The same scaled differential conductance plot taken in the hole-doped regime for device no. 2 (cooldown no. 1), with raw data included in Extended Data Fig. 7.

Fig. 3). The four-probe measurement presented here eliminates the contact resistance and provides a better evaluation of the anisotropy. As seen in Fig. 1i, although R_{hard} and R_{easy} are close when $tWTe_2$ is electron doped, the two curves substantially deviate from each other when the doping is changed to the hole side. Similar behaviours were also observed in device no. 2 (Fig. 1j and Extended Data Fig. 4). Figure 1k shows plots of the anisotropy ratio, $\beta_{4p} \equiv R_{hard}/R_{easy}$, which approaches approximately 1,000 in the hole-doped region, an exceptionally large value. The intrinsic resistivity anisotropy may be estimated to be as large as almost 50 on the basis of an electrostatic simulation considering the effect of measurement geometry (Extended Data Fig. 5).

Both varying the doping to the electron side or warming up the sample (Extended Data Figs. 4 and 6) strongly suppress β_{4p} to near unity, indicating that the large transport anisotropy is an intrinsic low-temperature property of hole carriers. Indeed, the correlation between the anisotropy and the hole doping is clearly seen in Fig. 2a, in which we map out β_{4p} as a function of both V_{tg} and V_{bg} for device no. 1 at 1.8 K (see also Extended Data Fig. 6). The transition from a nearly isotropic phase to a highly anisotropic phase occurs when the hole carriers become dominant, regardless of the electric displacement field.

Conductance power laws

The strongly anisotropic phase of $tWTe_2$ exhibits robust power-law and scaling behaviours in the across-wire transport (Fig. 2b), in which currents flow perpendicular to the moiré stripes (that is, the wires). Figure 2c plots the measured across-wire conductance G at a selected gate voltage in the hole-doped regime, with a two-probe configuration shown in Fig. 2b. As seen in the log–log plot, $G \propto T^{\alpha}$, for T below about 30 K, with an exponent α of approximately 0.98 (or approximately 1.14) for device no. 1 (or no. 2) at the chosen gate voltages. To demonstrate scaling, we present differential conductance (dI/dV) measurements under varying both the d.c. source-drain bias (V) and T (Fig. 2d). For small enough bias, dI/dV develops plateaus, indicating that the conductance is controlled only by T via the power law. At high bias, all curves taken at different T merge together, with a trend that can be well captured by the 'same' power-law exponent α, that is, dI/d$V \propto V^{\alpha}$ (the dashed line). Indeed, in the scaled conductance plot (Fig. 2e), (dI/dV)/T^{α} versus eV/k_BT, all data points, taken in a parameter range wider than a decade in T and three decades in V, collapse into a single curve[18,19]. A similar collapse can be found in device no. 2 (Fig. 2f and Extended Data Fig. 7).

In Extended Data Fig. 8, we compare along-wire and across-wire conductance taken from device no. 1. More robust power laws are typically seen in the across-wire direction. We note that contact resistance plays an important role in the along-wire transport, as seen in nanotubes[18]. In practice, the moiré system in the contact region may be affected by distortions, strain, unintentional doping and other interface effects. By contrast, across-wire resistance at low T is dominated by the $tWTe_2$ bulk (see Extended Data Fig. 9), a much more uniform area.

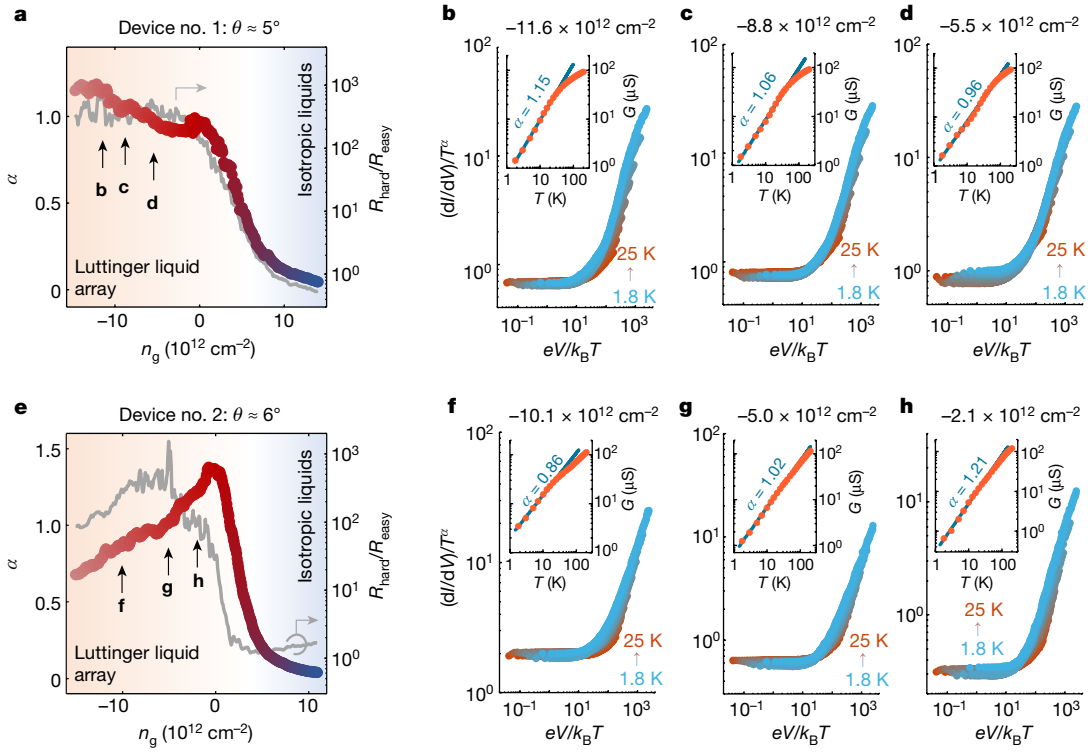

Fig. 3 | Gate-tuned power laws and anisotropy cross-over. a, Extracted power-law exponent α as a function of n_g based on temperature-dependent G (raw data in Extended Data Fig. 10), measured in device no. 1 (cooldown no. 2). The grey curve plots the measured anisotropy ratio on the basis of four-probe resistances along the easy and the hard direction in the same cooldown. **b**–**d**, The scaled differential conductance as a function of eV/k_BT at different n_g, indicated in **a**. Insets show the corresponding $G(T)$, from which the corresponding α is extracted on the basis of a power-law fit (solid line) to the low T data. Raw conductance data are shown in Extended Data Fig. 11. **e**–**h**, The same plots as in **b**–**d** but for device no. 2 (cooldown no. 2) with raw conductance data shown in Extended Data Figs. 10 and 12.

Gate-tuned anisotropy cross-over

The power-law across-wire conductance is generally observed over a wide range of gate voltages for $T < 30$ K in the $tWTe_2$ samples, as illustrated in Fig. 3 and Extended Data Figs. 10–12. We extract the n_g-dependent α together with β_{4p} for devices no. 1 and no. 2, respectively (Fig. 3a, e). In the hole-doped side, strong anisotropy occurs together with good power-law scaling characteristics, as shown by the collapse of the dI/dV curves over a wide range of T and V in the scaled plots (Fig. 3b–d for device no. 1; Fig. 3f–h for device no. 2). Although in both devices α is valued near unity on the hole side, the exact gate-dependent behaviour differs, which could arise owing to twist-angle-dependent electronic structures or extrinsic effects, such as disorders. Near charge neutrality or on the electron-doped regime, high-bias data deviate from the power-law trend (Extended Data Figs. 11 and 12). With electron doping, transport anisotropy is strongly suppressed, although zero-bias $G(T)$ still approximately follows a power law with a decreasing exponent down to near zero at high electron doping (Extended Data Fig. 10).

Band structure modelling

We further perform a continuum model analysis on $tWTe_2$ at the single-particle level (Fig. 4). The modelling is challenging, as even at the monolayer level, topology[20–23], correlations[16,17,24,25] and spin–orbit coupling[20] are all present. We start with a density functional theory (DFT) calculation on the monolayer, yielding valence band maximum at Γ flanked by two conduction band minima at the wavevector $\pm q_c$ (Fig. 4a). DFT calculations for untwisted but shifted bilayers are used to extract effective interlayer couplings (Fig. 4b, c), which enter the continuum model for obtaining the $tWTe_2$ structure[26]. The resulting twisted bands arising from one conduction valley are shown in Fig. 4d, in which a pair of highly anisotropic bands indeed develop in the hole regime, in contrast to the electron regime for which no substantial anisotropy is seen. Figure 4f illustrates the corresponding quasi-1D hole Fermi surface with the corresponding real space wavefunctions that coincide with the moiré stripes (Fig. 4e). In contrast to the $\pm q_c$ valleys, the moiré reconstruction of the valence bands at Γ is much less pronounced in this simplified model and develops no large anisotropy (Methods). Note that, although our simple analysis here does capture the emergence of quasi-1D bands, a comprehensive modelling would necessarily require future efforts involving large-scale DFT calculations, lattice reconstructions and interaction effects.

The Luttinger liquid interpretation

The large resistance anisotropy and contrasting T dependence of R_{hard} and R_{easy} (Extended Data Fig. 4) indicate that transport is qualitatively different between across- (insulating) and along-wire (metallic) directions. The power-law behaviour itself is inconsistent with the formation of an ordinary band or Mott insulator. The exponent α varies smoothly as a function of n_g, showing no obvious presence of a fully insulating state (Fig. 3), consistent with the absence of a gap in the modelling. For a 2D diffusive metal[27,28], the 'tunnelling anomaly' owing to the relaxation of injected charges at the contact may lead to a conductance power law depending on T or V. However, this cannot give distinct transport exponents in different directions and cannot account for our observation along the hard direction, where the resistance is dominated by the $tWTe_2$ bulk rather than contact effects. For disordered quasi-1D systems, calculations have shown that variable

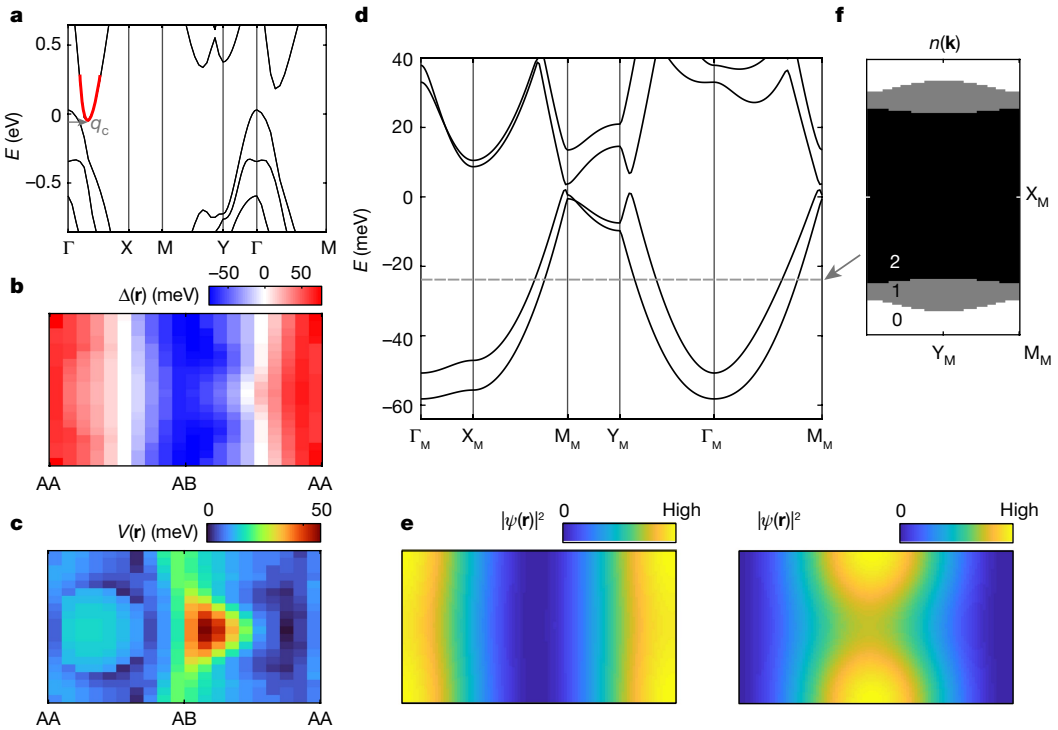

Fig. 4 | Theoretical modelling and the emergence of quasi-1D moiré bands at the single-particle level. a, DFT band structure for monolayer WTe_2. Red shading highlights the conduction band valleys at $\pm q_c$, about which the continuum model analysis in **b**–**f** is performed. Results are shown for one of the valleys. Energies are measured relative to the Fermi energy at charge neutrality. **b**,**c**, Interlayer hopping (**b**) and potential terms (**c**) plotted in the moiré unit cell. These quantities are extracted from DFT calculations of untwisted bilayers with in-plane shift $\mathbf{d} \approx \theta \hat{z} \times \mathbf{r}$, valid for a rigidly twisted $tWTe_2$. AA and AB indicate the positions of W superlattice chains (see Fig. 1b). **d**, Continuum model band structure for a conduction band valley, plotted along a cut in the moiré BZ. On hole doping, the system enters a highly anisotropic regime induced by the moiré physics. **e**, Representative Bloch wavefunctions in the quasi-1D regime plotted in the moiré unit cell. **f**, Illustrations of the quasi-1D open Fermi surfaces for moderate hole doping, with the number of occupied quasi-1D bands indicated.

range hopping transport may produce an apparent power-law behaviour[29], that is, $G \propto T^{\alpha}$ for $eV << k_BT$ and $dI/dV \propto V^{\beta}$ for $k_BT << eV$, where α and β are two generally unequal exponents that are independently controlled by microscopic details including disorder. This is, however, in sharp contrast to our observation in $tWTe_2$, where the power laws in T and V are controlled by the same exponent, namely, $\alpha = \beta$. This single-exponent scaling behaviour is robustly observed over a wide hole-doping range (Fig. 3 and Extended Data Figs. 11 and 12), where α has been tuned, and in samples with varied twist angles (devices no. 1 and no. 2). These observations provide strong evidence that the single-exponent power-law behavior is generic to the anisotropic phase of $tWTe_2$. Any explanation that requires fine-tuning of parameters to achieve the condition of $\alpha = \beta$ is unlikely to be feasible.

A natural explanation is emergent LL physics. The characteristic feature of a 1D LL in transport is indeed the 'single-exponent' power-law dependence of its conductance, that is, $\alpha = \beta$. The power-law transport of LL physics has been observed in several 1D systems, such as nanotubes[18,19,30,31], engineered 1D structures[31–33], edge modes[34–36], polymers[37] and self-organized gold wires[38]. However, extending LL physics from a single 1D wire to a 2D system is of fundamental interest yet challenging. Proposals to do so on the basis of 2D arrays of 1D wires have been put forward[2–6], but, as far as we know, the intriguing concept of a 2D anisotropic phase that mimics a LL has so far not been established in real materials.

Our observations on the hole side of $tWTe_2$ are well consistent with the generic LL expectations. We therefore propose that the anisotropic phase arises because of the formation of a 2D array of 1D LLs induced by the moiré superlattice. Understanding the moiré-induced LL behaviours in $tWTe_2$ requires proper consideration of electron interactions and transport mechanisms. In a quasi-1D system, although the early calculations[39] of the across-wire transport exponent between parallel LLs indicated $\alpha = 2\eta$, where η (which vanishes without interactions) is the Fermi surface exponent for an individual wire determined by the LL parameter K, the more recent consensus is instead that $\alpha = 2\eta - 1$, where the extra −1 arises from the fact that hopping can occur anywhere along the wires[40]. The relationship applies when single-particle hopping is the dominant conduction process and T is much larger than the 1D to 2D cross-over temperature $T^* \approx t_\perp (t_\perp/t_\parallel)^{\eta/(1-\eta)}$, where $t_\perp (t_\parallel)$ is the inter- (intra-) wire hopping[40]. From the energy scales of quasi-1D bands obtained in Fig. 4d, we may estimate $t_\perp \approx 5$ and $t_\parallel \approx 50$ meV, respectively. If this applies, for certain hole doping of $tWTe_2$ the across-wire conductance exhibits a power-law exponent $\alpha \approx 1$, corresponding to an effective $\eta \approx 1$, near the marginal boundary above which the single-particle process is no longer relevant and two-particle processes may be important. Assuming spin degeneracy and $\eta = (K + 1/K - 2)/4$ (ref. [40]), we obtain an effective intrawire $K \approx 0.17$ for $\alpha \approx 1$. The strong intrawire interaction is consistent with the experimental fact that the deviation from the power law is absent down to at least 1.8 K. This remarkably stable LL behaviour in the anisotropic 2D system calls for careful consideration of the interaction-driven phases in $tWTe_2$, especially the interwire interactions given the nanoscale wire spacing. Considering interwire interactions, the transport exponent then depends on a stiffness function $\kappa(q_\perp)$ instead of a single intrawire parameter K, where $q_\perp$ is the momentum perpendicular to the wires[3–6]. We note that further experimental and theoretical explorations are necessary to examine the exact connection between the measured power laws to interactions in the system, which is critical to evaluate the enticing possibility of a sliding LL phase and a host of competing orders descending from it[2–6].

Summary

We demonstrate a new tuneable platform based on tWTe_2 stacks for studying high-quality 2D arrays of 1D electronic structures in a crystalline superlattice. We interpret the results on the basis of the formation of a 2D anisotropic non-Fermi liquid phase that resembles a LL. An exciting direction is to search for new quantum Hall states with an applied magnetic field[4,7,8]. The physics of spin–charge separation[1,31,32], naturally expected in LLs, is another interesting direction to pursue. Experimental searches for evidence of spin–charge separation in a 2D WTe_2 system could provide important opportunities for studying new regimes in strongly correlated quantum phases.

Online content

Any methods, additional references, Nature Research reporting summaries, source data, extended data, supplementary information, acknowledgements, peer review information; details of author contributions and competing interests; and statements of data and code availability are available at https://doi.org/10.1038/s41586-022-04514-6.

1. Giamarchi, T. Quantum Physics in One Dimension (Oxford Univ. Press, 2003).
2. Wen, X. G. Metallic non-Fermi-liquid fixed point in two and higher dimensions. *Phys. Rev. B* **42**, 6623–6630 (1990).
3. Emery, V. J., Fradkin, E., Kivelson, S. A. & Lubensky, T. C. Quantum theory of the smectic metal state in stripe phases. *Phys. Rev. Lett.* **85**, 2160–2163 (2000).
4. Sondhi, S. L. & Yang, K. Sliding phases via magnetic fields. *Phys. Rev. B* **63**, 054430 (2001).
5. Vishwanath, A. & Carpentier, D. Two-dimensional anisotropic non-Fermi-liquid phase of coupled Luttinger liquids. *Phys. Rev. Lett.* **86**, 676–679 (2001).
6. Mukhopadhyay, R., Kane, C. L. & Lubensky, T. C. Sliding Luttinger liquid phases. *Phys. Rev. B* **64**, 045120 (2001).
7. Kane, C. L., Mukhopadhyay, R. & Lubensky, T. C. Fractional quantum Hall effect in an array of quantum wires. *Phys. Rev. Lett.* **88**, 036401 (2002).
8. Teo, J. C. Y. & Kane, C. L. From Luttinger liquid to non-Abelian quantum Hall states. *Phys. Rev. B* **89**, 085101 (2014).
9. Tam, P. M. & Kane, C. L. Nondiagonal anisotropic quantum Hall states. *Phys. Rev. B* **103**, 035142 (2021).
10. Neupert, T., Chamon, C., Mudry, C. & Thomale, R. Wire deconstructionism of two-dimensional topological phases. *Phys. Rev. B* **90**, 205101 (2014).
11. Iadecola, T., Neupert, T., Chamon, C. & Mudry, C. Wire constructions of Abelian topological phases in three or more dimensions. *Phys. Rev. B* **93**, 195136 (2016).
12. Meng, T., Neupert, T., Greiter, M. & Thomale, R. Coupled-wire construction of chiral spin liquids. *Phys. Rev. B* **91**, 241106 (2015).
13. Patel, A. A. & Chowdhury, D. Two-dimensional spin liquids with Z_2 topological order in an array of quantum wires. *Phys. Rev. B* **94**, 195130 (2016).
14. Kennes, D. M., Xian, L., Claassen, M. & Rubio, A. One-dimensional flat bands in twisted bilayer germanium selenide. *Nat. Commun.* **11**, 1124 (2020).
15. Ali, M. N. et al. Large, non-saturating magnetoresistance in WTe_2. *Nature* **514**, 205–208 (2014).
16. Wang, P. et al. Landau quantization and highly mobile fermions in an insulator. *Nature* **589**, 225–229 (2021).
17. Jia, Y. et al. Evidence for a monolayer excitonic insulator. *Nat. Phys.* **18**, 87–93 (2022).
18. Bockrath, M. et al. Luttinger-liquid behaviour in carbon nanotubes. *Nature* **397**, 598–601 (1999).
19. Yao, Z., Postma, H. W. C., Balents, L. & Dekker, C. Carbon nanotube intramolecular junctions. *Nature* **402**, 273–276 (1999).
20. Qian, X., Liu, J., Fu, L. & Li, J. Quantum spin Hall effect in two-dimensional transition metal dichalcogenides. *Science* **346**, 1344–1347 (2014).
21. Fei, Z. et al. Edge conduction in monolayer WTe_2. *Nat. Phys.* **13**, 677–682 (2017).
22. Tang, S. et al. Quantum spin Hall state in monolayer 1T′-WTe_2. *Nat. Phys.* **13**, 683–687 (2017).
23. Wu, S. et al. Observation of the quantum spin Hall effect up to 100 kelvin in a monolayer crystal. *Science* **359**, 76–79 (2018).
24. Sajadi, E. et al. Gate-induced superconductivity in a monolayer topological insulator. *Science* **362**, 922–925 (2018).
25. Fatemi, V. et al. Electrically tunable low-density superconductivity in a monolayer topological insulator. *Science* **362**, 926–929 (2018).
26. Jung, J., Raoux, A., Qiao, Z. & MacDonald, A. H. Ab initio theory of moiré superlattice bands in layered two-dimensional materials. *Phys. Rev. B* **89**, 205414 (2014).
27. Levitov, S. & Shytov, A. V. Semiclassical theory of the Coulomb anomaly. *J. Exp. Theor. Phys. Lett.* **66**, 214–221 (1997).
28. Bartosch, L. & Kopietz, P. Zero bias anomaly in the density of states of low-dimensional metals. *Eur. Phys. J. B* **28**, 29–36 (2002).
29. Rodin, A. S. & Fogler, M. M. Apparent power-law behavior of conductance in disordered quasi-one-dimensional systems. *Phys. Rev. Lett.* **105**, 106801 (2010).
30. Ishii, H. et al. Direct observation of Tomonaga–Luttinger-liquid state in carbon nanotubes at low temperatures. *Nature* **426**, 540–544 (2003).
31. Deshpande, V. V., Bockrath, M., Glazman, L. I. & Yacoby, A. Electron liquids and solids in one dimension. *Nature* **464**, 209–216 (2010).
32. Auslaender, O. M. et al. Spin-charge separation and localization in one dimension. *Science* **308**, 88–92 (2005).
33. Sato, Y. et al. Strong electron-electron interactions of a Tomonaga-Luttinger liquid observed in InAs quantum wires. *Phys. Rev. B* **99**, 155304 (2019).
34. Glattli, D. C. In *The Quantum Hall Effect: Poincaré Seminar 2004* (eds. Douçot, B. et al.) 163–197 (Birkhäuser, 2005); https://doi.org/10.1007/3-7643-7393-8_5.
35. Li, T. et al. Observation of a helical Luttinger liquid in InAs/GaSb quantum spin Hall edges. *Phys. Rev. Lett.* **115**, 136804 (2015).
36. Stühler, R. et al. Tomonaga–Luttinger liquid in the edge channels of a quantum spin Hall insulator. *Nat. Phys.* **16**, 47–51 (2020).
37. Biermann, S., Georges, A., Giamarchi, T. & Lichtenstein, A. In *Strongly Correlated Fermions and Bosons in Low-Dimensional Disordered Systems* (eds. Lerner, I. V et al.) 81–102 (Springer, 2002); https://doi.org/10.1007/978-94-010-0530-2_5.
38. Dudy, L., Aulbach, J., Wagner, T., Schäfer, J. & Claessen, R. One-dimensional quantum matter: gold-induced nanowires on semiconductor surfaces. *J. Phys. Condens. Matter* **29**, 433001 (2017).
39. Clarke, D. G., Strong, S. P. & Anderson, P. W. Incoherence of single particle hopping between Luttinger liquids. *Phys. Rev. Lett.* **72**, 3218–3221 (1994).
40. Georges, A., Giamarchi, T. & Sandler, N. Interchain conductivity of coupled Luttinger liquids and organic conductors. *Phys. Rev. B* **61**, 16393–16396 (2000).